Journal of Energy Storage 80 (2024) 110201

Contents lists available at ScienceDirect

Journal of Energy Storage

journal homepage: www.elsevier.com/locate/est

Research papers

Investigation on gas generation and corresponding explosion characteristics of lithium-ion batteries during thermal runaway at different charge states

Jiabo Zhang [a], Qianzhen Guo [a], Shaoyan Liu [c], Chao Zhou [a], Zhen Huang [a,b], Dong Han [a,b,*]

[a] Key Laboratory for Power Machinery and Engineering, Ministry of Education, Shanghai Jiao Tong University, Shanghai 200240, China
[b] Shanghai Non-carbon Energy Conversion and Utilization Institute, Shanghai 200240, China
[c] China-UK Low Carbon College, Shanghai Jiao Tong University, Shanghai, 200240, China

ARTICLE INFO

Keywords:
Lithium-ion battery safety
Thermal runaway
State of charge
Gas generation
Explosion limit

ABSTRACT

This study investigates the gas generation characteristics and explosion limits of the gas generated by 18650-type $LiNi_{1/3}Co_{1/3}Mn_{1/3}O_2$ (NCM) cells during thermal runaway (TR) at different states of charge (SOCs). An accelerating rate calorimeter is employed to initialize TR, together with an airtight jar for gas measurement. Based on the detected gas composition for NCM cells, the corresponding explosion limits are computed and further compared with those of $LiFePO_4$ (LFP) and $LiNi_{0.80}Co_{0.15}Al_{0.05}O_2$ (NCA) cells. The results reveal that the gas generation rates are slightly higher for NCM cells with lower SOCs prior to the violent TR processes compared to those for high-SOC cells, primarily due to the elevated reaction temperature. Moreover, during violent TR, multiple-peak features are observed for the gas generation rate curves, especially at high-SOC conditions. On the other hand, typical Z-shaped explosion limit curves are observed for all generated mixtures. As the cathode material varies from NCM to LFP and NCA, the explosion limits shift from high-temperature regions to low-temperature regions. In contrast to common beliefs that the generation gas at high SOCs is more explosive, non-monotonic responses of the explosion limit curves are found with respect to cell SOC. The significance of minor components of the generated gas, including ethylene and ethane, in reducing the explosivity of the mixture, is highlighted through sensitivity analyses.

1. Introduction

Lithium-ion batteries (LIBs) offer a promising solution for a low-carbon, sustainable future, owing to their high energy density, good cycling performance, and low self-discharge rate [1,2]. As LIB technology continues to advance, it is increasingly being applied across various fields, i.e., electric vehicles (EVs), energy storage systems (ESSs), and aviation propulsion [3–5]. However, the development of LIBs is restricted due to safety concerns. At mechanical, electrical, and thermal abuse conditions, LIBs may fall into a so-called thermal runaway (TR) process [6]. During TR, uncontrollable side reactions could occur between the reactive materials inside LIB, including cathode/anode, separator, and electrolyte [7–9]. A large amount of heat and flammable gas is generated simultaneously, leading to high fire and explosion risks [10,11].

The heat generation characteristics during TR have been extensively studied based on thermal analyses. It is widely adopted that the TR process is featured by three characteristic temperatures, namely the onset temperature of TR, the separator collapse temperature, and the maximum temperature [10,12]. Accordingly, the TR processes are separated into three key stages, and the heat released during each stage is modeled by Arrhenius-like expressions [13–16]. In addition to the temperature rise, TR also leads to a rapid generation of gas, which significantly increases the pressure inside the LIB, potentially resulting in the opening of the safety valve and the following explosion risk of the combustible gas. Despite the safety hazards associated with gas generation during TR, there is limited understanding of the underlying gas generation mechanisms.

To reveal the pressure evolution of LIB at TR, the LIB sample is usually sealed in an airtight canister equipped with pressure sensors [17–20]. While this method is capable of measuring the total amount of gas generated, it faces the drawback that the in-cell pressure prior to the LIB safety valve opening is lacking. However, this information holds critical significance in the early warning of TR, going beyond typical TR monitoring methods based solely on internal battery electrical characteristics [21,22]. By introducing the gas generation characteristics as a new metric into the TR warning of the battery management system (BMS), significant advantages are achieved in

* Corresponding author at: Key Laboratory for Power Machinery and Engineering, Ministry of Education, Shanghai Jiao Tong University, Shanghai 200240, China.
E-mail address: dong_han@sjtu.edu.cn (D. Han).

https://doi.org/10.1016/j.est.2023.110201
Received 22 October 2023; Accepted 18 December 2023
Available online 3 January 2024
2352-152X/

terms of advanced warning timing and high sensitivity of TR detection, which helps to improve the safety of LIBs [23,24]. To this end, Qin et al. [25] developed a new method to detect the full-cycle pressure trace of a sample LIB by cutting off the top hat of the cell and sealing it inside a canister. By this mean, the gas release characteristics of a commercial 18650-type $LiNi_{0.8}Co_{0.1}Mn_{0.1}O_2$ cell were studied using an accelerating rate calorimeter (ARC). The results revealed that, prior to the separator collapse temperature, the generated gas came from both electrolyte evaporation and redox side reactions, and the gas generation rate was not linearly related to the temperature rise. In a subsequent investigation, Jia et al. [26] examined the effects of cathode materials, including $LiFePO_4$ (LFP), $LiMn_2O_4$ (LMO), and NCM, on the gas release behavior of fully-charged LIBs. It was found that the order of gas release amount before the cell approached the separator collapse temperature was LFP > NCM > LMO cells. Further, Mao et al. [27] experimentally tested the gas generation features for NCM cells. The amount of gas generated was approximately 10 mmol before the opening of the safety valve, and the peak pressure could reach as high as 2.566 MPa. The multi-stage kinetics parameters of gas generation processes at different stages were also developed with respect to the heat release rates. However, the full-cycle investigations of TR processes are limited; in particular, the detailed evolution of gas generation rate and amount of TR at each stage for cells with different states of charge (SOCs), has not been fully disclosed.

In addition to the gas generation rate and pressure trace during TR, the generated gas composition is also of importance [28,29]. This is because the high-temperature gas vented from the ruptured cell would rapidly mix with the surrounding air, potentially leading to fire hazards through either forced ignition or autoignition [30]. Notable incidents include the explosion of a train car in Houston, Texas in April 2017, attributed to the presence of the LIBs being transported to a recycling facility. The force of the explosion shattered windows of buildings located 500 ft away [31]. In April 2019, an explosion occurred in a 2 MW LIB ESS system at a solar facility in Surprise, AZ, resulting in injuries to eight firefighters [32]. Moreover, in April 2021, a 25 MWh LIB ESS in downtown Beijing, China experienced a devastating explosion, claiming the lives of three individuals [33]. To gain more insights of the combustible gas, a gas chromatograph (GC) was employed by Golubkov et al. [34], and the composition of the generated gas of LFP and $LiNi_{0.80}Co_{0.15}Al_{0.05}O_2$ (NCA) cells at different SOCs. H_2, CH_4, CO, CO_2, C_2H_4, and C_2H_6 were found as the main contributors of the generated gas, regardless of the cell type and SOC, but the proportions were found quantitatively different. Similarly, Shen et al. [35] compared the generated gas composition between LFP and NCM cells after TR. It was found that LFP cells produced more H_2 than NCM cells, which may lead to a higher fire risk.

For a specific mixture, its explosivity is controlled by chemical kinetics [36,37], and the explosion response may be non-monotonic with ambient conditions. Taking H_2/O_2 mixture as an example, a well-known Z-shaped explosion limit curve was observed [38], in which the mixture is explosive, non-explosive, and explosive again with the increase of pressure at moderate temperature. As the generated gas of TR includes H_2 and many other reactive components, the interactions between different chemical kinetics make the prediction of explosion limits challenging. Recently, Yu et al. [39] gave a first attempt to evaluate the explosion limits of generated gas for NCA cells at different SOCs. The typical Z-shaped curves were observed under all considered conditions, which demonstrated the dominance of H_2 in the explosion response. However, due to the quantitative difference in the gas composition, the effects of cathode materials on the explosion limits of the generated gas remain largely unknown.

Motivated by the above considerations, the objectives of the present study are two-fold: (1) to investigate the effects of SOCs on gas generation characteristics of NCM cells throughout the full-cycle TR processes, and (2) to quantitatively evaluate the explosivity of the generated gas of NCM cells at varied SOCs and compare it with that of cells having different cathode materials. In particular, commercial 18650-type $LiNi_{1/3}Co_{1/3}Mn_{1/3}O_2$ cells, with top hats removed, were sealed in an airtight jar and further conducted TR tests in an accelerating rate calorimeter (ARC). Five different SOCs, ranging from 30% to 120%, were considered. According to the characteristic temperatures, three stages of gas generation processes were categorized. The effects of SOC on the gas generation rates and amounts at different stages were as such studied. Moreover, the explosion limits of the generated gas of NCM cells at different SOCs were quantitatively analyzed and compared with those of LFP and NCA cells.

Table 1
Summary of the tested LIB characteristics.

Sample cells	Parameters
Dimensions (mm)	18 (diameter) ×65 (height)
Cell weight (g)	46
Cathode material	NCM 111
Anode material	Graphite
Composition of electrolyte	1M $LiPF_6$ -DEC:EMC:EC
Rated capacity (mAh)	2500
Nominal voltage (V)	3.7
State of Charge	120%, 100%, 70%, 50%, 30%

DEC: diethyl carbonate; EMC: ethyl methyl carbonate; EC: ethylene carbonate.

2. Experimental setup and methods

2.1. Experimental setup

2.1.1. The tested cell samples

The LIB cells used in this study were commercial 18650-type NCM batteries (Shenzhen Doublepow Technology Co., Ltd., China), with a diameter of 18 mm and a length of 65 mm. The detailed parameters of the studied batteries are listed in Table 1. Specifically, the cathode and anode materials were $LiNi_{1/3}Co_{1/3}Mn_{1/3}O_2$ (NCM 111) and natural graphite, respectively. The main components of the electrolyte were diethyl carbonate (DEC), ethyl methyl carbonate (EMC), and ethylene carbonate (EC), with the salts of $LiPF_6$. The fresh cells were first fully charged to rate their capacity (used 1 A current to charge to the nominal voltage of 3.7 V and then constant-voltage charged until the current decayed to less than 40 mA). Note that the cells were charged and discharged three times for rating their capacity and then recharged to the desired SOCs by setting the ratio between charged capacity and the rated capacity. Five SOCs were selected in this study, namely 120%, 100%, 70%, 50%, and 30%, respectively. The maximum SOC of 120% is selected as a representative overcharged condition, which may trigger TR through electrical abuse [40]. On the contrary, the minimum SOC of 30% is employed, given that this threshold typically aligns with the safe shipment requirement for LIBs [41]. Following the completion of the charging process, a stabilization period of 24 h was ensured for the cell before proceeding with the experimental procedures.

2.1.2. Experimental apparatus

The schematic diagram of the experimental apparatus used in this study is depicted in Fig. 1. Specifically, an accelerating rate calorimeter (ARC, Hangzhou YOUNG Instruction Science & Technology Co., Ltd., China) was employed to measure the TR behavior of cells with different SOCs. The ARC allows the typical heat-wait-seek (H-W-S) mode to accurately capture the onset temperature of TR and guarantee a uniform equilibrium state during the TR process. Moreover, a stainless airtight jar was positioned within the ARC to facilitate the measurement of gas generation characteristics throughout the TR process. The stainless airtight jar has an inner radius of 39 mm and a height of 68 mm, which allows a maximum pressure of 20 MPa. As the main gas generation process of TR is generally rapid [27], the pressure transducer was set to detect the inner pressure of the jar with a high frequency of 1000 Hz. To ensure accurate temperature measurements, the frequency

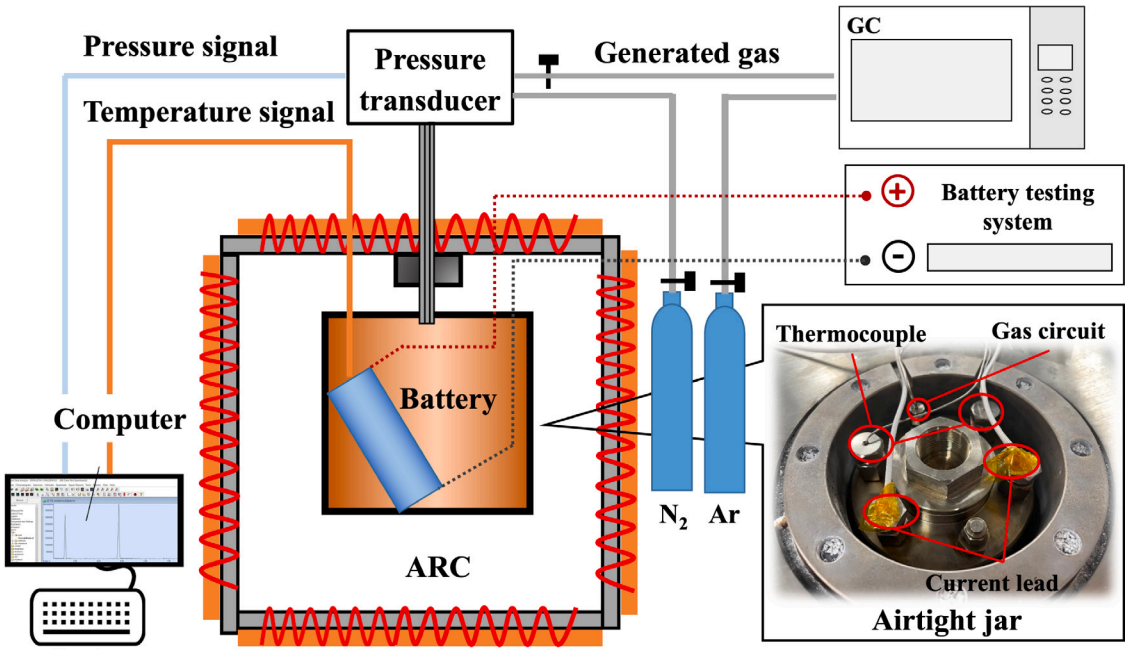

Fig. 1. Schematic of the experimental setup for temperature, pressure, voltage, and generated gas measurement during the thermal runaway process of LIB.

of temperature measurement is set at 1 Hz in consideration of the required time for the thermal couple to reach thermal equilibrium with its surrounding environment. This frequency is deemed sufficient according to Jia et al. [26] to capture the relatively slower temperature changes compared to pressure variations. Moreover, the margin of error for temperature and pressure measurements is estimated to be ±10%, as confirmed by multiple repetitions of experiments.

On the other hand, voltage is crucial as it provides insights into the electrochemical properties of the cell. In this study, the voltage is monitored by externally connecting the current leads to the electrodes within the airtight jar. A battery testing system (CT-4008-5V20A-A, Shenzhen Neware Technology Co., Ltd., China) is further employed for the real-time detection of voltage changes during the TR process. The gaseous and solid mass losses of the cell are also measured to characterize the extent of material decomposition during TR. Moreover, to analyze the composition of the generated gas, a flame ionization detector (FID) was connected to a GS-Alumina column in a gas chromatograph (GC, Agilent 7890B) to measure C1–C2 hydrocarbons, such as CH_4, C_2H_4, and C_2H_6, while a thermal conductivity detector (TCD) was employed for the detection of permanent gas, such as H_2, CO, CO_2, H_2O, and O_2.

2.1.3. Experimental methods

The experiments followed the below procedures using the setup as shown in Fig. 1.

I. The gas circuits within the system, including ARC and the airtight jar, were first back-flashed using N_2 to create an inert gas environment.
II. To measure the gas generation and pressure evolution characteristics during the entire LIB TR process, the top hat and safety valve of the cell was removed by a cutter bar in a N_2-filled glove box.
III. In the glove box, the cut cell was put inside the airtight jar with an N-type thermocouple attached to its surface for temperature measurement. Additionally, current leads were connected to the anode and cathode of the cell. These connections facilitated the transmission of temperature and voltage signals outside the jar through gas-tight ports.
IV. The airtight jar was then sealed and connected to the ARC via a gas circuit through another gas-tight port, and the pressure signal was collected using a pressure transducer. Note that, the voltage is measured by connecting the current leads to a battery testing system.
V. The heat-wait-seek (H-W-S) mode was used to initiate the TR process, with an increasing temperature step of 5 K. Note that the temperature rate sensitivity to detect the self-heating of the cell was 0.01 K·min^{-1}.
VI. During TR, ARC followed the detected temperature of the cell, in which a quasi-adiabatic condition was achieved. The output temperature and pressure signals were recorded.
VII. After TR, the gas generated was collected and the corresponding components were measured by a gas chromatograph (GC, Agilent 7890B). The gaseous and solid mass losses were simultaneously recorded to characterize the extent of material decomposition and gas generation during TR.

Note that, in order to ensure the robustness and accuracy of the experimental data, the cell TR tests for each SOC condition were conducted in a repeated manner, with a minimum of three repetitions for cross-validation.

2.2. Numerical methods

2.2.1. Gas generation analysis

In this study, the actual volume of the airtight jar, V_a, can be expressed as:

$$V_a = V_{jar} - V_c + V_{void}, \tag{1}$$

where V_{jar} is the inner volume of the jar of 3.25×10^{-4} m^3, V_c is the volume of the tested cell of 1.65×10^{-5} m^3, and V_{void} is the void space within the test cell ($V_{void} = 0.07V_c$ [25]).

The inert gas (primarily N_2) amount, n_0, in a mole basis, is obtained from the initial state,

$$n_0 = \frac{V_a P_0}{R_g T_0}, \tag{2}$$

where T_0 and P_0 are the initial temperature and pressure within the jar, respectively; R_g is the gas constant of 8.314 J·mol^{-1}·K^{-1}.

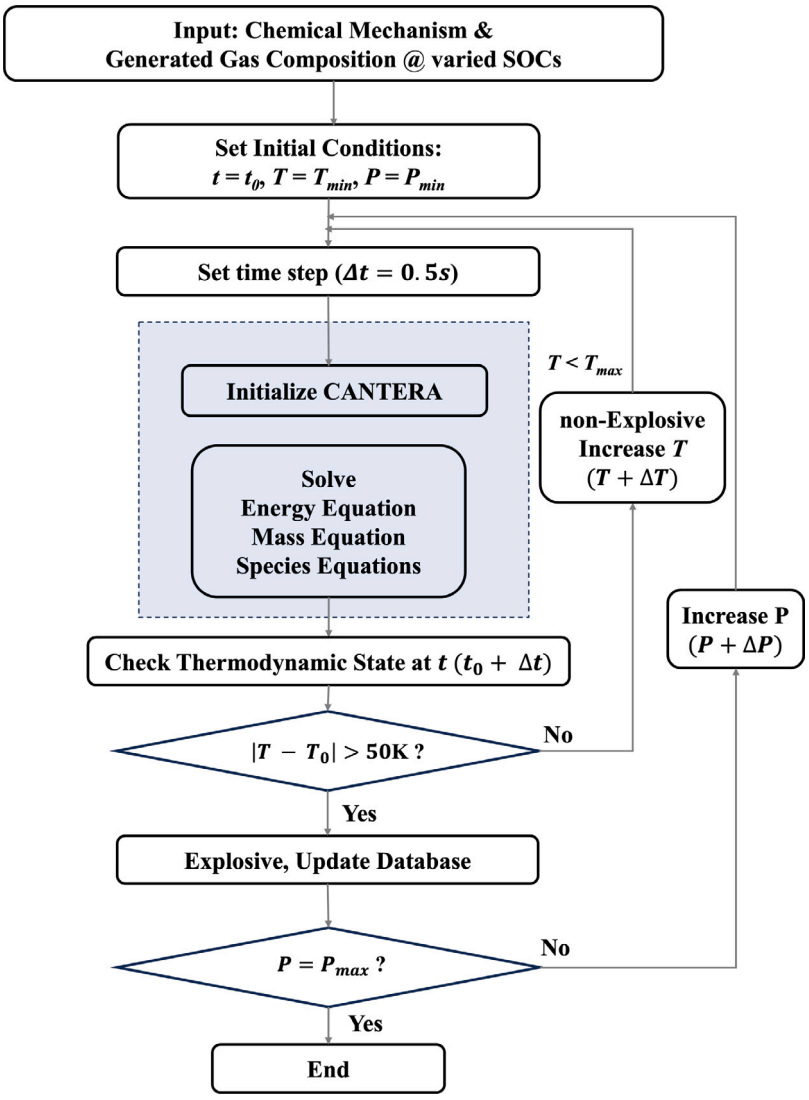

Fig. 2. Calculation flowchart of explosion limits for the generated gas during thermal runaway.

The amount of generated gas, n_g, during the TR process, is assumed to obey the ideal gas equation [25–27] and can be calculated by:

$$n_g = \frac{V_a P}{Z_g R_g T} - n_0, \tag{3}$$

where Z_g is the compressible factor of the generated gas. As the compressibility of the major generated gas, including H_2, CO, CO_2, etc., is around 1 [42,43], $Z_g = 1$ is selected in this study. Consistent with Jia et al. [26] and Mao et al. [27], the temperature data in this study is linearly interpolated to match the high-frequency pressure data to compute the gas generation amount in Eq. 3. Note that n_g includes both the evaporated electrolyte solvents and the generated gas by side chemical reactions. As the electrolyte solvents vapor may participate in the side reactions at any moment, these two terms are not analyzed separately as in [27].

2.2.2. Explosion limit evaluation

The main components of the generated gas include H_2, CH_4, CO, CO_2, C_2H_4, and C_2H_6 [33,34]. After TR, the high-temperature generated gas could quickly mix with the ambient air. The high-explosive mixture may ignite and causes serious safety issues. The explosion is governed by the chemical kinetic characteristics of the mixture. Therefore, an accurate chemical kinetic mechanism is necessary to evaluate the explosion limits. Recently, Yu et al. [39] compared the performance of five widely-used mechanisms, namely the Aramco 2.0 mech. [44], C_1/C_3 mech. [45], LLNL mech. [46], San Diego mech. [47], and NUIG Mech1.1 [48], on calculating the explosion limits of LIB TR generated gas. Among these mechanisms, NUIG Mech1.1 [48] provided the most reasonable prediction with the tested explosion limits and was as such employed in this study.

Fig. 2 illustrates the flowchart in calculating explosion limits. First, the selected chemical mechanism and the detected generated gas composition were inputted into the homemade code. Second, the Cantera library [49] was initialized to set the initial thermodynamic parameters. After solving the energy, mass, and species equations, the temperature rise within a specific time step, Δt, was obtained. Note that, the explosion criterion of a 50 K temperature increase, $|T - T_0| > 50$ K, within 0.5 s [50] was employed to identify if the mixture is explosive. Finally, to explore the explosion limits at various conditions, the code iterated through a wide range of temperatures spanning from 300 K to 2000 K and pressures spanning from 1×10^2 Pa to 1×10^7 Pa. Employing the above code, the explosion limits of different generated gas for NCM cells with varied SOCs were investigated and further compared with those of NCA and LFP cells [34,39]. To avoid complexity, the generated gas/O_2 mixtures were all set as stoichiometric states.

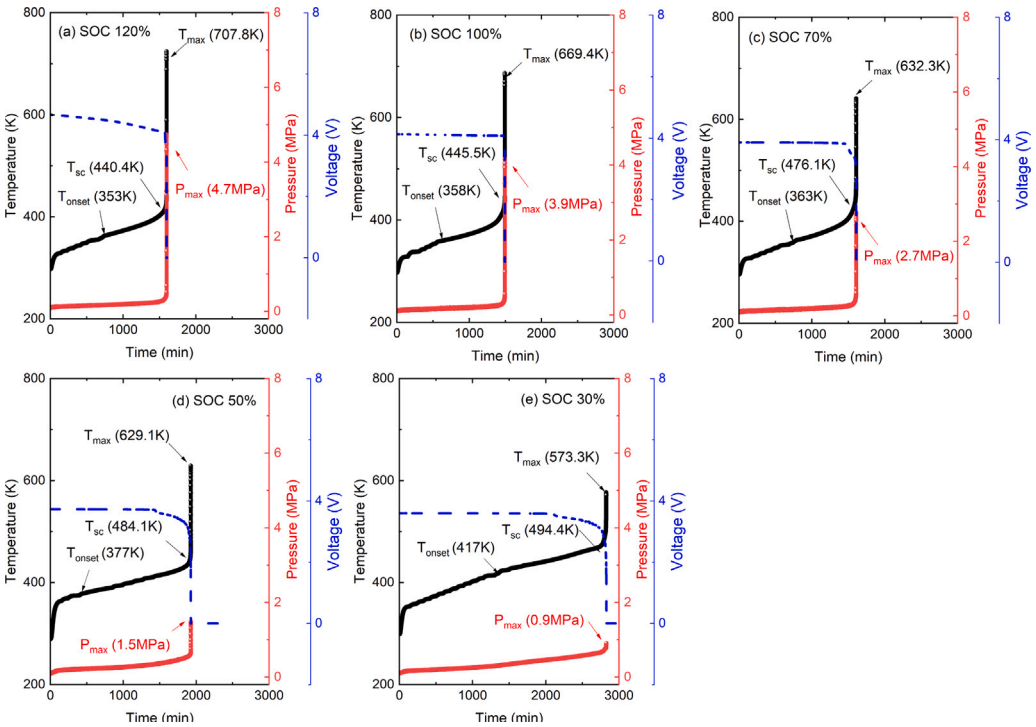

Fig. 3. Evolution of temperature, pressure and voltage for NCM cells with different SOCs: (a) SOC 120%, (b) SOC 100%, (c) SOC 70%, (d) SOC 50%, and (e) SOC 30%.

2.3. Innovation and practical applications

In this study, an ARC was employed in combination with an airtight jar to simultaneously measure the temperature and pressure evolution inside LIBs with varied SOCs during TR. Note that the jar used in this study is of larger dimensions compared to the one used in previous studies [25]. By using this redesigned jar, the limitations where the internal pressure rapidly exceeded the maximum allowable pressure of the jar due to the violent TR, leading to jar rupture, are overcome. Moreover, the top hat and safety valve of the cell was removed before the TR test. This allows the direct detection of gas generation information of cells prior to the venting behavior. Therefore, a comprehensive investigation of the full-cycle TR processes, including its early stages, was undertaken. From practical aspects, the obtained data on gas generation rate and amount prior to the violent TR presents a novel metric for TR early warning [23,24]. In pack-level applications, the battery management system (BMS) can take essential actions upon identifying signals of increased internal pressure emanating from individual cell TR.

On the other hand, once TR is triggered, the highly explosive generated gas could mix with the surrounding air and potentially lead to thermal hazards [41]. Therefore, the explosivity of the generated gas was numerically evaluated. Note that, both atmospheric and sub-atmospheric conditions are considered in this study, as LIBs are also widely used in aviation propulsion systems operating at low pressures. As reported by the Federal Bureau of Investigation (FBI), a notable occurrence of 308 aviation accidents worldwide occurred between 2006 and 2021, highlighting the necessity of evaluating the potential thermal risks [51]. Additionally, studies conducted by Fu et al. [52] and Xie et al. [53] demonstrated that altitude increase could result in a lower onset temperature for TR, exacerbating its severity under low pressures. In light of these concerns, the explosivity of the vented gas is investigated and compared at a wide range of thermodynamic conditions to align with more practical applications.

3. Results and discussion

3.1. Overall thermal runaway behavior for cells with different SOCs

The evolution of surface temperature, inside-jar pressure, and voltage for cells with different SOCs is plotted in Fig. 3. As mentioned in the experimental procedures, the top heads of the cells are removed to detect the entire gas generation process. Consequently, the temperature drop typically caused by the venting cooling effect resulting from the opening of the safety valve is not observed. Consistent with the findings of Feng et al. [12], three key thermal characteristic temperatures, $\{T_{onset}, T_{sc}, T_{max}\}$, are readily observed to describe the TR processes for all cells. Specifically, T_{onset} is the onset temperature for the self-heating of the cell, T_{sc} is the separator collapsing temperature, and T_{max} is the maximum temperature. Note that T_{onset} monotonically increases from 353 K to 417 K with SOC decreasing from 120% to 30%. This is reasonable as T_{onset} is controlled by the SEI decomposition from the anode [54]. A decreased SOC results in an increase in cell thermal stability, and thus increases T_{onset}. During a long self-heating period of $\sim \mathcal{O}(1000)$ mins, the cell temperature gradually increases and finally reaches T_{sc}, in which the rapid heat release stage of TR is initiated [40]. Similar to T_{onset}, T_{sc} is generally higher for cells with lower SOCs. After the temperature reaches T_{sc}, a large amount of heat is generated within a few seconds, leading the cell to reach T_{max}. Note that T_{max} is decreased with decreased SOC, indicating the corresponding cell is less reactive with suppressed exothermic reactions. Moreover, it is readily observed that the voltage change aligns well with the distinct stages of the TR process characterized by $\{T_{onset}, T_{sc}, T_{max}\}$. Starting from T_{onset}, the voltage progressively decreases, signifying the degradation of the associated electrochemical property. Note that, for the cell with a SOC of 120%, the voltage begins to decline before T_{onset}. This is reasonable as the cell is in a transitional state towards electronic equilibrium for overcharged cells. Beyond T_{SC}, the voltage drops to near 0 V, indicating a complete cell failure.

On the other hand, the pressure experiences a smooth increase before the temperature reaches T_{sc}, suggesting less amount of gas is

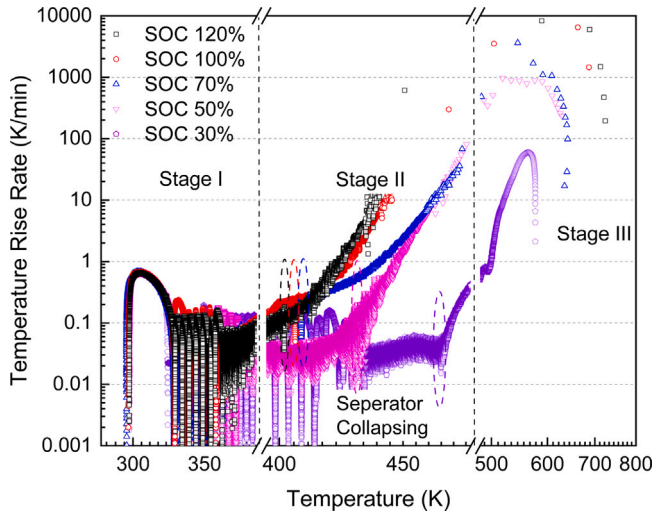

Fig. 4. The temperature rise rate, dT/dt, as a function of cell temperature for NCM cells with different SOCs.

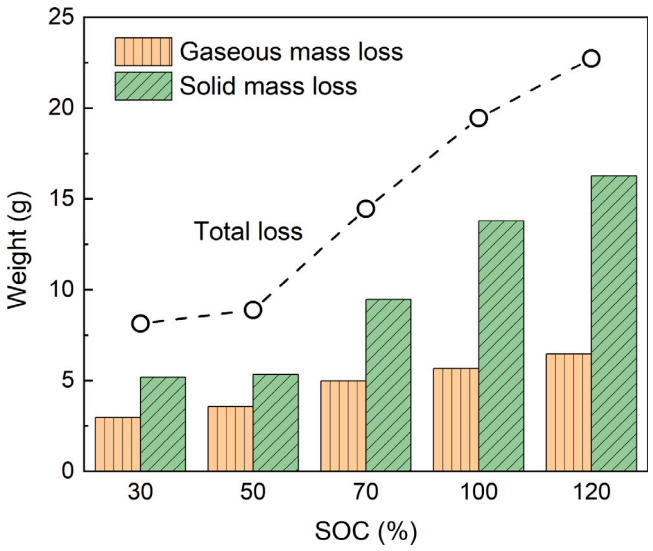

Fig. 5. The gaseous and solid mass losses as a function of SOC for NCM cells after thermal runaway.

generated before T_{sc}. However, after T_{sc}, the pressure rapidly increases to its peak magnitude, P_{max}. Moreover, the variations for P_{max} between cells with different SOCs are much more obvious than those of T_{max}, indicating the total amount of released gas greatly differs with various SOCs.

As shown in Fig. 4, the temperature rise rate, dT/dt, as a function of cell temperature, is further illustrated for cells with different SOCs. Three stages are distinguished based on the temperature matrix $\{T_{onset}, T_{sc}, T_{max}\}$. Stage I refers to the heating process before cell temperature reaches T_{onset}. In this Stage, dT/dt by cell self-heating is less than 0.01 K/min, and thus the ARC could homogeneously increase the ambient temperature with a step of 5 K until T_{onset} is reached. Further, in Stage II, cells undergo stable self-heating processes with $dT/dt >$ 0.1 K/min, and the magnitude of dT/dt increases with increased SOC. Note that, during Stage II, drops of dT/dt for cells with different SOCs are observed with transient $dT/dt <$ 0.1 K/min. This is primarily due to the collapse of the cell separator [55]. As an endothermic reaction, the separator collapsing leads to an endothermic valley [56].

After the failure of the separator, the direct contact between cathode and anode materials leads to a continuously dramatic rise of the dT/dt, and the violent TR process (Stage III) is triggered. As demonstrated by Feng et al. [12], Stages II and III are separated by the critical temperature for instantaneous large amounts of heat releasing. In Stage III, the maximum magnitude of dT/dt is achieved, and it decreases with decreasing SOCs. Taking the SOC 120% cell as an example, the cell temperature rapidly increases from ~ 450 K to ~ 700 K with $(dT/dt)_{max}$ of $\mathcal{O}(10^4)$ K·min^{-1}. On the contrary, for the SOC 30% cell, $(dT/dt)_{max}$ decreases to $\mathcal{O}(10^2)$ K·min^{-1} with T_{max} of ~ 600 K.

Moreover, gaseous and solid mass losses are individually quantified after TR, as depicted in Fig. 5. The results highlight a monotonically increasing trend in mass loss with respect to SOC. Specifically, the total mass loss is relatively low for cells with SOC lower than 50%. As SOC increases from 50% to 120%, the total mass loss increases by approximately a factor of two, indicating a more complete reactive material decomposition within the cell. Further, solid mass loss is identified to be the primary contributor to the total mass loss in comparison to the gaseous mass loss.

3.2. Gas generation characteristics for cells with different SOCs

Despite the presence of inert gas, the pressure within the airtight jar primarily increases due to the evaporation of the electrolyte and subsequent side chemical reactions [12,41]. Therefore, the vapor pressure of the electrolyte, P_{ele}, is first decoupled from the pressure generated by side reactions, P_g, to identify the occurrence of TR. Specifically, without gas generation due to side reactions, P_{ele} is assumed to be equal to the saturation pressure of the electrolyte at the vapor–liquid equilibrium (VLE), P_{sat}, as represented by Eq. (4).

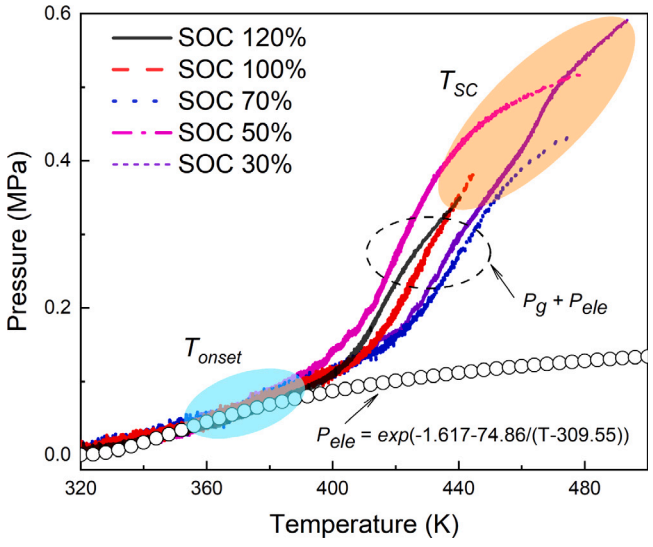

Fig. 6. The partial pressure before T_{sc} due to P_{ele} and P_g as a function of temperature for NCM cells with different SOCs.

$$P_{ele} = P_{sat} = e^{a-\frac{b}{T-c}}, \tag{4}$$

where P_{sat} obeys Antoine's equation [25,29,57] with $a = -1.617$, $b = 74.86$, and $c = 309.55$ for the present set of data.

The partial pressure before T_{sc} due to P_{ele} and P_g as a function of temperature for NCM cells with different SOCs is plotted in Fig. 6. It is evident that, prior to T_{onset} (Stage I), P_{ele} stands as the exclusive factor contributing to the total pressure increase. In this phase, P_{ele} is equal to the saturation pressure of the electrolyte at the vapor–liquid equilibrium (VLE), signifying the absence of side reactions. As for Stage II, side reactions gradually manifest, accompanied by an increase in P_g. Moreover, cells with lower SOCs typically exhibit higher P_g at T_{SC}, indicating the side reactions are more complete side reactions occurring at the point of separator collapsing.

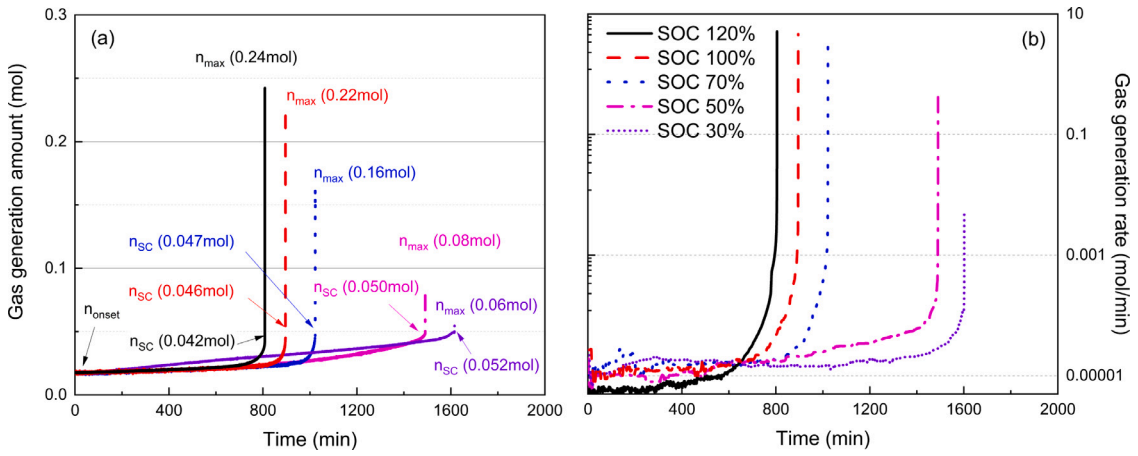

Fig. 7. The gas generation (a) amount and (b) rate evolution for NCM cells with different SOCs after the temperature reaches T_{onset}.

With the above understanding, the gas generation amounts and rates for cells with different SOCs are plotted in Figs. 7 a and b, respectively. Note that the gas generated in Stage I is negligible, as the side reactions during TR have not occurred and the generated gas is primarily due to the evaporation of the electrolyte [26]. Therefore, Fig. 7 tracks the gas generation profiles from T_{onset} to T_{max}. Several points are made from this figure.

First, during Stage II, the generated gas smoothly increases for all cells with $dn/dt \in [1\times10^{-5}, 1\times10^{-4}]$ mol/min, indicating a mild gas generation process prior to the violent TR processes. Moreover, dn/dt is generally higher for cells with lower SOCs during Stage II. This is reasonable as T_{onset} increases with decreased SOC (see Fig. 3). An increased temperature could increase the reactivity of the side reactions and as such enhance dn/dt. Second, the gas generation amount at T_{sc}, n_{sc}, experiences a slight increase from 0.042 mol to 0.052 mol with SOC decreasing from 120% to 30%. This difference is caused by the extended duration of Stage II with reduced SOC. In Stage II, the primary gas generation reactions include the decomposition of the solid electrolyte interface (SEI) film, cathode/anode materials breakdown, and their interactive reactions with the electrolyte [58]. An extended duration of Stage II leads to more thorough progress of the above reactions, which slightly increases n_{sc}. Third, in Stage III, a large amount of gas is generated from n_{sc} to n_{max} within a few seconds for cells with 120%, 100%, and 70% SOCs. In contrast, the variation between n_{sc} and n_{max} is much smaller for the 50% and 30% SOC cells. This is reasonable as the primary contributor to gas generation in Stage III is the combustion of the flammable electrolyte [58]. Due to the prolonged duration of Stage II, the electrolyte consumes more before the violent TR processes, leading to less gas generation in Stage III for cells with lower SOCs.

Fig. 8 further illustrates the amounts of gas generation and corresponding gas generation rates, dn/dt, for cells with different SOCs during Stage III. It is readily observed that, for 120%, 100%, and 70% SOC cells, a dramatic amount of gas is released within 5 s with a comparable $(dn/dt)_{max}$ of ~10 mol/min. Note that multiple-peak features are observed for the dn/dt curves, especially for cells with higher SOCs. This indicates that the gas generation process in Stage III may not be fully described with a single-step-reaction assumption. This is consistent with the observations in the literature. During the violent TR, the decomposition of cathode materials and subsequent reactions with the electrolyte are the primary contributors to heat release and gas generation [10,52]. As reported by Kim et al. [59,60], the decomposition process of NCM materials exhibits two exothermic peaks, which necessitates the use of two sets of kinetic parameters to describe the electrolyte–cathode reaction in numerical simulations [61]. However, for cells at low-SOC states, the limited availability of lithium ions in the

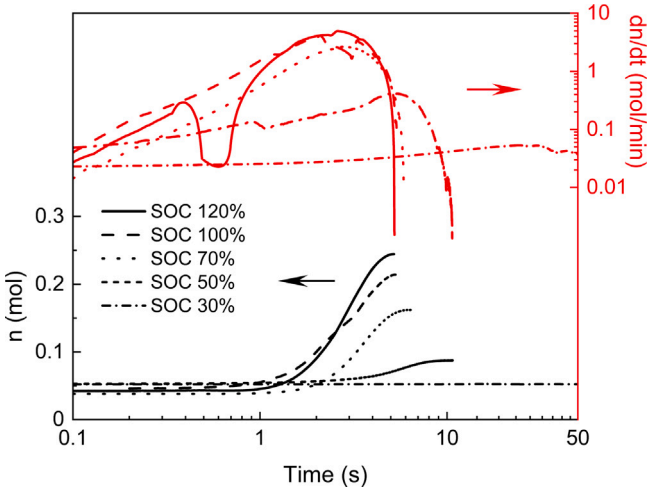

Fig. 8. The amounts of gas generation and gas generation rates for NCM cells with different SOCs during Stage III.

cathode material suppresses the occurrence of multi-staged cathode–electrolyte reactions, resulting in a single-peak gas generation profile. Moreover, for cells with lower SOCs, namely 50% SOC and 30% SOC, the gas generation process is smoother compared to those with higher SOCs. Specifically, for the 30% SOC cell, n_{max} of 0.06 mol is gradually achieved with a prolonged duration with $dn/dt < 0.1$ mol/min.

Finally, the generated gas during TR is collected and examined by a GC. The corresponding gas compositions for NCM cells with different SOCs are given in Fig. 9. For a side-by-side comparison, the generated gas composition for LIBs tested by Golubkov et al. [34] with different cathode materials, such as LFP and NCA, are plotted simultaneously. Note that the gas components plotted in Fig. 9 account for more than 98% of the total gas. Three major gas generation components, namely H_2, CO, and CO_2, are found for cells with different cathode materials as shown in Fig. 9 a. Overall, NCM and LFP cells have comparable generated gas composition, in which CO_2 is the primary contributor, followed by H_2 and CO. On the contrary, for NCA cells, CO rather than CO_2 is the main component of the generated gas, indicating that the oxidizability of the NCA cells is lower than the NCM and LFP cells. Moreover, with an increased SOC, the concentration of CO_2 decreases, while those for H_2 and CO increase. On the other hand, Fig. 9 b illustrates other minor components of the generated gas, including CH_4, C_2H_4, and C_2H_6. For NCM and NCA cells, the concentration of CH_4 is found higher than those of C_2H_4 and C_2H_6. As for LFP cells, more

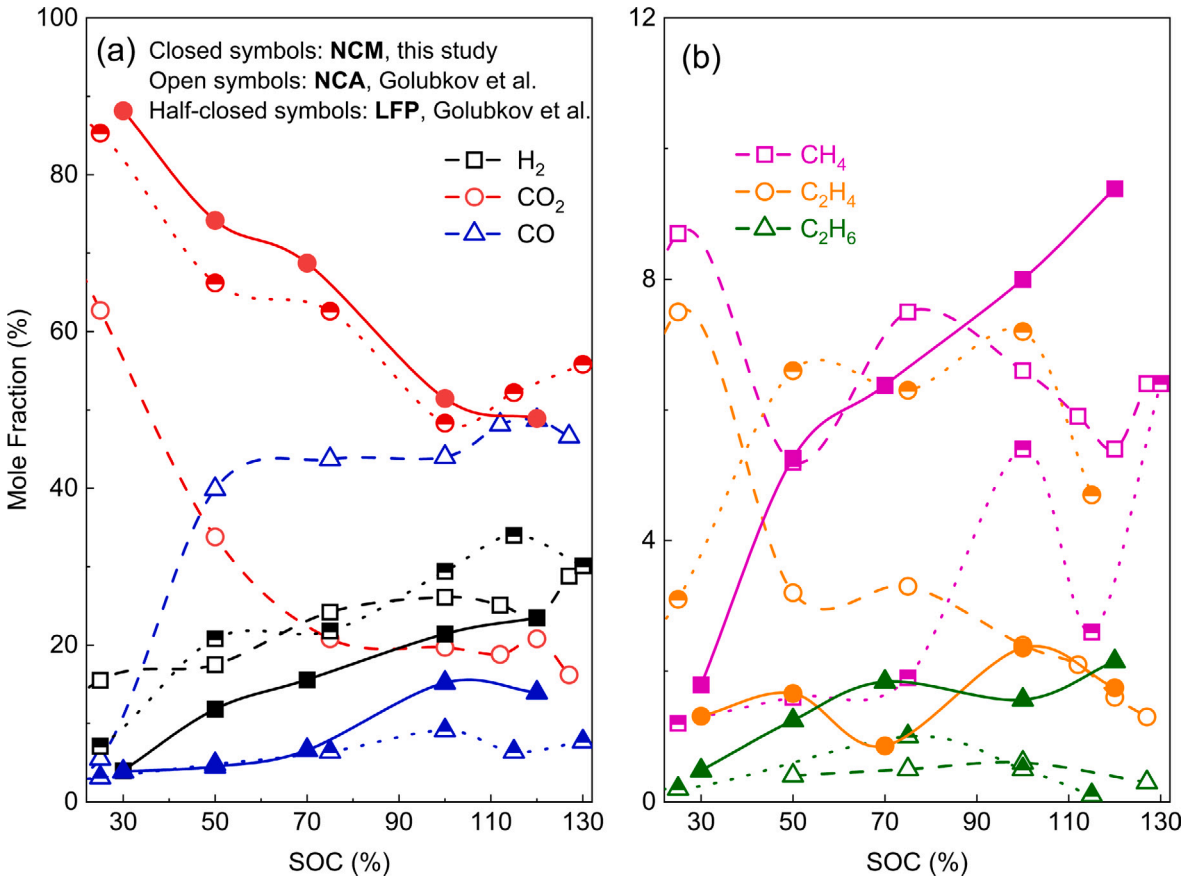

Fig. 9. The generated gas compositions of NCM (this study), NCA [34] and LFP [34] cells with different SOCs: (a) major components and (b) minor components.

C_2H_4 could be generated, followed by CH_4 and C_2H_6. However, non-monotonic relationships are found between these minor component concentrations and cell SOC.

3.3. Explosion limits of generated gas for different cells

Next, according to the tested gas composition as shown in Fig. 9, the pressure–temperature explosion limits of the generated gas for NCM, NCA, and LFP cells at different SOCs are plotted in Fig. 10. Note that the explosion limits of the generated gas of 30% SOC cell are not included in this study. This is because approximately 90% of the gas composition is composed of CO_2 (see Fig. 9), which is inert and non-explosive. Several points are made from Fig. 10. First, for all the studied generated gas, typical Z-shaped explosion limit curves are observed. Specifically, at moderate temperatures, the generated gas is sequentially non-explosive, explosive, non-explosive, and explosive again as pressure increases. Consequently, the Z-shaped non-monotonic response segments the diagram into the first, second, and third limits in the low-, middle-, and high-pressure regimes, respectively. Second, the Z-shaped explosion limits shift significantly from the high-temperature region to the low-temperature region as the cathode material varies from NCM to LFP and NCA. This indicates that the generated gas of NCA cells is the most explosive, followed by LFP cells and NCM cells. According to the gas composition in Fig. 9, NCA cells generate the highest amount of reactive gas, including H_2 and CO. These components dominate over the reactivity of the mixture, which agrees well with the observations from Yu et al. [39]. Third, as a general trend, the gas generated by a cell with a higher SOC is more explosive. For example, as the SOC increases from 50% to 100%, the explosion limit curve shifts to the low-temperature and low-pressure regions for NCA cells. However, for NCM cells, the explosion temperature moves

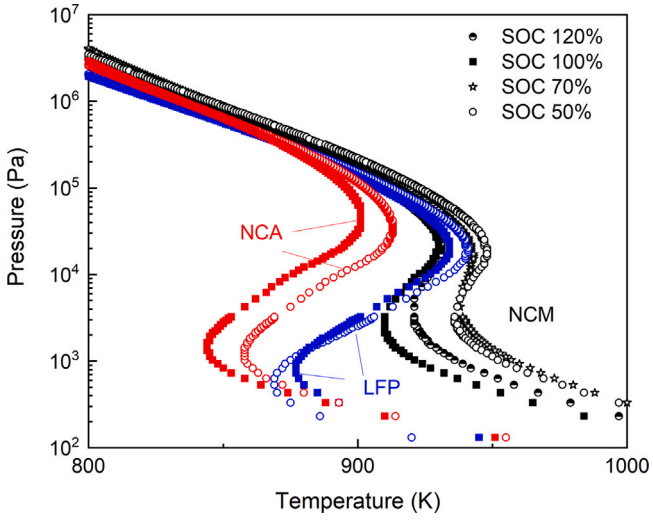

Fig. 10. Comparison of explosion limits of the stoichiometric generated gas/O_2 mixtures for NCM, NCA and LFP cells with different SOCs.

to the high-temperature region as the SOC increases from 100% to 120%. Similarly, for LFP cells, the first explosion limit shifts upwards as the SOC increases from 50% to 100%. These are inconsistent with the assumption that mixtures containing higher proportions of highly reactive components, such as H_2, have higher explosivity.

To explain the non-monotonic responses of the explosion limit curves with respect to cell SOC, sensitivity analyses are conducted to investigate the effects of gas composition on explosivity, as shown in

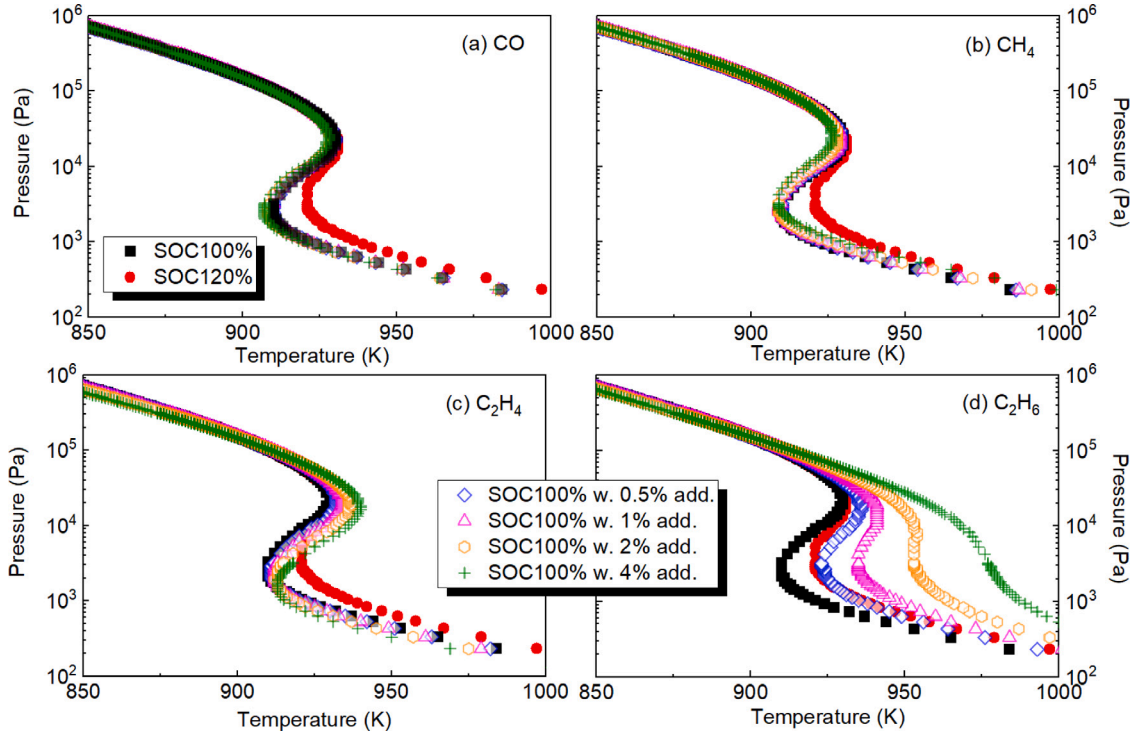

Fig. 11. Effects of minor generated gas components addition on the explosion limits of stoichiometric NCM cell generated gas/O_2 mixtures: (a) CO, (b) CH_4, (c) C_2H_4 and (d) C_2H_6.

Fig. 11. Specifically, with the addition of 0.5% to 4% of reactive components other than H_2 (i.e. CO, CH_4, C_2H_4, and C_2H_6), the variations of explosion limit of the generated gas for NCM cell at 100% SOC are studied. The explosion limit of the generated gas for NCM cell at 120% SOC is plotted simultaneously as a reference (red color). As shown in Figs. 11 a and b, with up to 4% addition of CO and CH_4, the explosion limit of the NCM SOC 100% cell generated gas is nearly unchanged, indicating the fractions of these two species are insensitive to the explosivity of the mixture. Moreover, with the addition of C_2H_4 (Fig. 11 c), the explosion limit curve of the NCM SOC 100% cell generated gas shifts to the high-temperature regimes with a reduced second explosion pressure limit. As for C_2H_6 (Fig. 11 d), its addition leads to a most significant change in the first and second explosion pressure limits, indicating its strong influence on the explosivity of the mixture. With a slight addition of 0.5%, the explosivity of the mixture is significantly suppressed, which is comparable with that of the SOC 120% mixture. Further increasing the additional proportion of C_2H_6 to 4.0%, the Z-shaped explosion limit transits to a monotonic trend, being more explosive with increasing temperature and pressure. These findings suggest that the explosivity of the generated gas is not solely determined by the concentration of H_2, and other reactive species in the gas composition also play an important role, especially C_2H_4 and C_2H_6. As a slight variation (~0.5%) of these gas compositions could lead to a significant change in the explosion limits, the reaction pathway of C_2H_4 and C_2H_6 during TR should be focused. The possible reaction pathways include the decomposition of the SEI layer [62] and the anode–electrolyte reactions [41,63], as depicted in R1–R3.

$$(CH_2CH_2OCO_2Li)_2 = Li_2CO_3 + 2C_2H_4 + CO_2 + 0.5O_2 \quad \text{(R1)}$$

$$2Li + C_3H_4O_3(EC) = Li_2CO_3 + C_2H_4 \quad \text{(R2)}$$

$$2Li + C_3H_6O_3(DMC) = Li_2CO_3 + C_2H_6 \quad \text{(R3)}$$

For explosion safety considerations, the final generated amount of C_2H_4 and C_2H_6 should be examined carefully, and specific fire suppressants targeting on C_2H_4 and C_2H_6 can be useful for suppressing fire hazards.

4. Conclusions

In this study, experiments on the gas generation characteristics of NCM cells during thermal runaway (TR) at different states of charge (SOCs: 120%, 100%, 70%, 50%, and 30%) were conducted using an accelerating rate calorimeter (ARC) in combination with an airtight jar. The gas generation processes were categorized into three stages, namely Stage I to III, according to the thermal response of the cell based on the temperature matrix $\{T_{onset}, T_{sc}, T_{max}\}$. The effects of SOC on the gas generation rates and amount at different stages, including the stage prior to the violent TR, as well as the generated gas compositions after TR, were studied. Moreover, the explosion limits of the generated gas of NCM cells were analyzed and compared with those of LFP and NCA cells at a wide range of thermodynamic conditions. The main conclusions of the current study are as follows:

(1) The gas generation rates are slightly higher for NCM cells with lower SOCs prior to the violent TR processes compared to those for high-SOC cells, primarily due to the increased reaction temperature. Further, the gas generation amount at T_{sc}, n_{sc}, experiences a slight increase from 0.042 mol to 0.052 mol with SOC decreasing from 120% to 30%, which is primarily because of the prolonged duration of Stage II from T_{onset} to T_{sc}.

(2) A dramatic amount of gas is generated in Stage III from T_{sc} to T_{max} within a few seconds. A decrease in SOC leads to a reduced gas generation rate and gas generation amount, especially for the SOC 50% and 30% cells. Multiple-peak features are observed for the gas generation rate curves, indicating that the gas generation process in Stage III may not be fully described with a single-step-reaction assumption.

(3) The major generated gas components for NCM cells is CO_2, followed by H_2, CO, CH_4, C_2H_4, and C_2H_6, which is comparable with LFP cells. On the contrary, for NCA cells, CO rather than CO_2 is the main component of the generated gas, indicating that the oxidizability of the NCA cells is lower than the NCM and LFP cells. With the increase in SOC, the concentration of CO_2 decreases, while those for H_2 and CO increase.

(4) Typical Z-shaped explosion limit curves are observed for the generated gas of NCM, NCA, and LFP cells at different SOCs. The Z-shaped explosion limits shift from the high-temperature region to the low-temperature region as the cathode material varies from NCM to LFP and NCA. However, in contrast to common beliefs that the generation gas at high SOCs is more explosive, non-monotonic responses of the explosion limit curves are found with respect to cell SOC, especially at sub-atmospheric conditions. Through sensitivity analyses, it is revealed that a slight variation (~0.5%) of C_2H_4 or C_2H_6 proportion could significantly reduce the explosivity of the mixture, indicating their importance in evaluating the explosion safety.

CRediT authorship contribution statement

Jiabo Zhang: Conceptualization, Methodology, Investigation, Formal analysis, Data curation, Writing – original draft. **Qianzhen Guo:** Data curation, Visualization. **Shaoyan Liu:** Data curation, Methodology. **Chao Zhou:** Data curation. **Zhen Huang:** Supervision, Resources, Funding acquisition. **Dong Han:** Supervision, Funding acquisition, Writing – review & editing.

Declaration of competing interest

The authors declare that they have no known competing financial interests or personal relationships that could have appeared to influence the work reported in this paper.

Data availability

Data will be made available on request.

Acknowledgments

This research work is supported by the National Natural Science Foundation of China (Grant Nos. 52106261 and 52022058) and the Postdoctoral Research Foundation of China (Grant Nos. 2022M712042 and 2022T150403).

References

[1] W. He, W. Guo, H. Wu, L. Lin, Q. Liu, X. Han, Q. Xie, P. Liu, H. Zheng, L. Wang, X. Yu, D.-L. Peng, Challenges and recent advances in high capacity li-rich cathode materials for high energy density lithium-ion batteries, Adv. Mater. 33 (50) (2021) 2005937.

[2] X. Zhang, Z. Li, L. Luo, Y. Fan, Z. Du, A review on thermal management of lithium-ion batteries for electric vehicles, Energy 238 (2022) 121652.

[3] I. López, E. Ibarra, A. Matallana, J. Andreu, I. Kortabarria, Next generation electric drives for HEV/EV propulsion systems: Technology, trends and challenges, Renew. Sustain. Energy Rev. 114 (2019) 109336.

[4] D.D. Lecce, R. Verrelli, J. Hassoun, Lithium-ion batteries for sustainable energy storage: recent advances towards new cell configurations, Green Chem. 19 (15) (2017) 3442–3467.

[5] X. Yang, T. Liu, S. Ge, E. Rountree, C. Wang, Challenges and key requirements of batteries for electric vertical takeoff and landing aircraft, Joule 5 (7) (2021) 1644–1659.

[6] Y. Chen, Y. Kang, Y. Zhao, L. Wang, J. Liu, Y. Li, Z. Liang, X. He, X. Li, N. Tavajohi, B. Li, A review of lithium-ion battery safety concerns: The issues, strategies, and testing standards, J. Energy Chem. 59 (2021) 83–99.

[7] Q. Wang, P. Ping, X. Zhao, G. Chu, J. Sun, C. Chen, Thermal runaway caused fire and explosion of lithium ion battery, J. Power Sources 208 (2012) 210–224.

[8] J. Zhang, A. Zhong, Z. Huang, D. Han, Experimental and kinetic study on the stabilities and gas generation of typical electrolyte solvent components under oxygen-lean oxidation and pyrolysis conditions, Sci. China Technol. Sci. 65 (12) (2022) 2883–2894.

[9] Q. Guo, J. Zhang, C. Zhou, Z. Huang, D. Han, Thermal runaway behaviors and kinetics of NCM Lithium-ion batteries at different heat dissipation conditions, J. Electrochem. Soc. 170 (8) (2023) 080507.

[10] X. Feng, D. Ren, X. He, M. Ouyang, Mitigating thermal runaway of lithium-ion batteries, Joule 4 (4) (2020) 743–770.

[11] J. Duan, X. Tang, H. Dai, Y. Yang, W. Wu, X. Wei, Y. Huang, Building safe lithium-ion batteries for electric vehicles: A review, Electrochem. Energy. Rev. 3 (1) (2019) 1–42.

[12] X. Feng, S. Zheng, D. Ren, X. He, L. Wang, X. Liu, M. Li, M. Ouyang, Key characteristics for thermal runaway of li-ion batteries, Energy Procedia 158 (2019) 4684–4689.

[13] H. Chen, J.E. Buston, J. Gill, D. Howard, R.C. Williams, C.M.R. Vendra, A. Shelke, J.X. Wen, An experimental study on thermal runaway characteristics of lithium-ion batteries with high specific energy and prediction of heat release rate, J. Power Sources 472 (2020) 228585.

[14] P. Liu, Y. Li, B. Mao, M. Chen, Z. Huang, Q. Wang, Experimental study on thermal runaway and fire behaviors of large format lithium iron phosphate battery, Appl. Therm. Eng. 192 (2021) 116949.

[15] C. Jin, Y. Sun, H. Wang, X. Lai, S. Wang, S. Chen, X. Rui, Y. Zheng, X. Feng, H. Wang, M. Ouyang, Model and experiments to investigate thermal runaway characterization of lithium-ion batteries induced by external heating method, J. Power Sources 504 (2021) 230065.

[16] C.M. Vendra, A.V. Shelke, J.E. Buston, J. Gill, D. Howard, E. Read, A. Abaza, B. Cooper, J.X. Wen, Numerical and experimental characterisation of high energy density 21700 lithium-ion battery fires, Process Saf. Environ. Prot. 160 (2022) 153–165.

[17] S. Koch, A. Fill, K.P. Birke, Comprehensive gas analysis on large scale automotive lithium-ion cells in thermal runaway, J. Energy Storage 398 (2018) 106–112.

[18] F. Diaz, Y. Wang, R. Weyhe, B. Friedrich, Gas generation measurement and evaluation during mechanical processing and thermal treatment of spent Li-ion batteries, Waste Manag. 84 (2019) 102–111.

[19] Y. Zhang, H. Wang, W. Li, C. Li, M. Ouyang, Quantitative analysis of eruption process of abused prismatic Ni-rich automotive batteries based on in-chamber pressure, J. Energy Storage 31 (2020) 101617.

[20] L. Yuan, T. Dubaniewicz, I. Zlochower, R. Thomas, N. Rayyan, Experimental study on thermal runaway and vented gases of lithium-ion cells, Process Saf. Environ. Prot. 144 (2020) 186–192.

[21] Z. Liao, J. Zhang, Z. Gan, Y. Wang, J. Zhao, T. Chen, G. Zhang, Thermal runaway warning of lithium-ion batteries based on photoacoustic spectroscopy gas sensing technology, Int. J. Energy Res. 46 (15) (2022) 21694–21702.

[22] D. Kong, H. Lv, P. Ping, G. Wang, A review of early warning methods of thermal runaway of lithium ion batteries, J. Energy Storage 64 (2023) 107073.

[23] Y. Jin, Z. Zheng, D. Wei, X. Jiang, H. Lu, L. Sun, F. Tao, D. Guo, Y. Liu, J. Gao, Y. Cui, Detection of micro-scale Li dendrite via H_2 gas capture for early safety warning, Joule 4 (8) (2020) 1714–1729.

[24] P. Kaur, S. Bagchi, D. Gribble, V.G. Pol, A.P. Bhondekar, Impedimetric chemosensing of volatile organic compounds released from Li-ion batteries, ACS Sens. 7 (2) (2022) 674–683.

[25] P. Qin, J. Sun, Q. Wang, A new method to explore thermal and venting behavior of lithium-ion battery thermal runaway, J. Power Sources 486 (2021) 229357.

[26] Z. Jia, P. Qin, Z. Li, Z. Wei, K. Jin, L. Jiang, Q. Wang, Analysis of gas release during the process of thermal runaway of lithium-ion batteries with three different cathode materials, J. Energy Storage 50 (2022) 104302.

[27] B. Mao, C. Fear, H. Chen, H. Zhou, C. Zhao, P.P. Mukherjee, J. Sun, Q. Wang, Experimental and modeling investigation on the gas generation dynamics of lithium-ion batteries during thermal runaway, eTransportation 15 (2023) 100212.

[28] S. Chen, Z. Wang, J. Wang, X. Tong, W. Yan, Lower explosion limit of the vented gases from Li-ion batteries thermal runaway in high temperature condition, J. Loss Prev. Process Ind. 63 (2020) 103992.

[29] Z. Jia, S. Wang, P. Qin, C. Li, L. Song, Z. Cheng, K. Jin, J. Sun, Q. Wang, Comparative investigation of the thermal runaway and gas venting behaviors of large-format $LiFePO_4$ batteries caused by overcharging and overheating, J. Energy Storage 61 (2023) 106791.

[30] P. Liu, C. Liu, K. Yang, M. Zhang, F. Gao, B. Mao, H. Li, Q. Duan, Q. Wang, Thermal runaway and fire behaviors of lithium iron phosphate battery induced by over heating, J. Energy Storage 31 (2020) 101714.

[31] S. Beausoleil, Lithium batteries causes train car explosion in NE houston, 2017, https://www.khou.com/article/news/local/neighborhood-residents-concerned-following-train-car-explosion/285-433810198.

[32] A.R. Baird, E.J. Archibald, K.C. Marr, O.A. Ezekoye, Explosion hazards from lithium-ion battery vent gas, J. Power Sources 446 (2020) 227257.

[33] H. Wang, H. Xu, Z. Zhang, Q. Wang, C. Jin, C. Wu, C. Xu, J. Hao, L. Sun, Z. Du, Y. Li, J. Sun, X. Feng, Fire and explosion characteristics of vent gas from lithium-ion batteries after thermal runaway: A comparative study, eTransportation 13 (2022) 100190.

[34] A.W. Golubkov, S. Scheikl, R. Planteu, G. Voitic, H. Wiltsche, C. Stangl, G. Fauler, A. Thaler, V. Hacker, Thermal runaway of commercial 18650 Li-ion batteries with LFP and NCA cathodes – Impact of state of charge and overcharge, RSC Adv. 5 (70) (2015) 57171–57186.

[35] H. Shen, H. Wang, M. Li, C. Li, Y. Zhang, Y. Li, X. Yang, X. Feng, M. Ouyang, Thermal runaway characteristics and gas composition analysis of lithium-ion batteries with different LFP and NCM cathode materials under inert atmosphere, Electronics 12 (7) (2023) 1603.

[36] X. Wang, C.K. Law, An analysis of the explosion limits of hydrogen-oxygen mixtures, J. Chem. Phys. 138 (13) (2013) 134305.
[37] W. Liang, J. Liu, C.K. Law, On explosion limits of H_2/CO/O_2 mixtures, Combust. Flame 179 (2017) 130–137.
[38] C.K. Law, Combustion Physics, Cambridge University Press, 2010.
[39] R. Yu, J. Liu, W. Liang, C.K. Law, H. Wang, M. Ouyang, On explosion limits of NCA battery vent gas, Proc. Combust. Inst. (2022) http://dx.doi.org/10.1016/j.proci.2022.11.010.
[40] X. Feng, S. Zheng, D. Ren, X. He, L. Wang, H. Cui, X. Liu, C. Jin, F. Zhang, C. Xu, H. Hsu, S. Gao, T. Chen, Y. Li, T. Wang, H. Wang, M. Li, M. Ouyang, Investigating the thermal runaway mechanisms of lithium-ion batteries based on thermal analysis database, Appl. Energy 246 (2019) 53–64.
[41] Q. Wang, B. Mao, S.I. Stoliarov, J. Sun, A review of lithium ion battery failure mechanisms and fire prevention strategies, Prog. Energy Combust. Sci. 73 (2019) 95–131.
[42] Z. Chen, Y. Qin, Y. Ren, W. Lu, C. Orendorff, E.P. Roth, K. Amine, Multi-scale study of thermal stability of lithiated graphite, Energy Environ. Sci. 4 (10) (2011) 4023.
[43] J.K. Ostanek, W. Li, P.P. Mukherjee, K. Crompton, C. Hacker, Simulating onset and evolution of thermal runaway in Li-ion cells using a coupled thermal and venting model, Appl. Energ. 268 (2020) 114972.
[44] W.K. Metcalfe, S.M. Burke, S.S. Ahmed, H.J. Curran, A hierarchical and comparative kinetic modeling study of C1–C2 hydrocarbon and oxygenated fuels, Int. J. Chem. Kinet. 45 (10) (2013) 638–675.
[45] H. Hashemi, J.M. Christensen, S. Gersen, H. Levinsky, S.J. Klippenstein, P. Glarborg, High-pressure oxidation of methane, Combust. Flame 172 (2016) 349–364.
[46] R. Seiser, H. Pitsch, K. Seshadri, W. Pitz, H. Gurran, Extinction and autoignition of n-heptane in counterflow configuration, Proc. Combust. Inst. 28 (2) (2000) 2029–2037.
[47] Chemical-kinetic mechanisms for combustion applications, san diego mechanism web page, mechanical and aerospace engineering (combustion research), 2014, URL http://combustion.ucsd.edu.
[48] M. Baigmohammadi, V. Patel, S. Nagaraja, A. Ramalingam, S. Martinez, S. Panigrahy, A.A.E.-S. Mohamed, K.P. Somers, U. Burke, K.A. Heufer, A. Pekalski, H.J. Curran, Comprehensive experimental and simulation study of the ignition delay time characteristics of binary blended methane, ethane, and ethylene over a wide range of temperature, pressure, equivalence ratio, and dilution, Energ. Fuels 34 (7) (2020) 8808–8823.
[49] D.G. Goodwin, H.K. Moffat, R.L. Speth, Cantera: An object-oriented software toolkit for chemical kinetics, thermodynamics, and transport processes, Caltech, Pasadena, CA (2009).
[50] Y. Liu, D. Han, Numerical study on explosion limits of ammonia/hydrogen/oxygen mixtures: Sensitivity and eigenvalue analysis, Fuel 300 (2021) 120964.
[51] Y. Liu, H. Niu, Z. Li, J. Liu, C. Xu, X. Huang, Thermal runaway characteristics and failure criticality of massive ternary Li-ion battery piles in low-pressure storage and transport, Process Saf. Environ. Prot. 155 (2021) 486–497.
[52] Y. Fu, S. Lu, L. Shi, X. Cheng, H. Zhang, Ignition and combustion characteristics of lithium ion batteries under low atmospheric pressure, Energy 161 (2018) 38–45.
[53] S. Xie, L. Ren, X. Yang, H. Wang, Q. Sun, X. Chen, Y. He, Influence of cycling aging and ambient pressure on the thermal safety features of lithium-ion battery, J. Power Sources 448 (2020) 227425.
[54] H.M. Barkholtz, Y. Preger, S. Ivanov, J. Langendorf, L. Torres-Castro, J. Lamb, B. Chalamala, S.R. Ferreira, Multi-scale thermal stability study of commercial lithium-ion batteries as a function of cathode chemistry and state-of-charge, J. Power Sources 435 (2019) 226777.
[55] X. Feng, M. Ouyang, X. Liu, L. Lu, Y. Xia, X. He, Thermal runaway mechanism of lithium ion battery for electric vehicles: A review, Energy Stor. Mater. 10 (2018) 246–267.
[56] S. Zheng, L. Wang, X. Feng, X. He, Probing the heat sources during thermal runaway process by thermal analysis of different battery chemistries, J. Power Sources 378 (2018) 527–536.
[57] P.T. Coman, S. Mátéfi-Tempfli, C.T. Veje, R.E. White, Modeling vaporization, gas generation and venting in Li-ion battery cells with a dimethyl carbonate electrolyte, J. Electrochem. Soc. 164 (9) (2017) A1858.
[58] Q. Wang, L. Jiang, Y. Yu, J. Sun, Progress of enhancing the safety of lithium ion battery from the electrolyte aspect, Nano Energy 55 (2019) 93–114.
[59] H.-S. Kim, M. Kong, K. Kim, I.-J. Kim, H.-B. Gu, Effect of carbon coating on $LiNi_{1/3}Mn_{1/3}Co_{1/3}O_2$ cathode material for lithium secondary batteries, J. Power Sources 171 (2) (2007) 917–921.
[60] H.-S. Kim, K. Kim, S.-I. Moon, I.-J. Kim, H.-B. Gu, A study on carbon-coated $LiNi_{1/3}Mn_{1/3}Co_{1/3}O_2$ cathode material for lithium secondary batteries, J. Solid State Electrochem. 12 (7–8) (2008) 867–872, http://dx.doi.org/10.1007/s10008-008-0552-0.
[61] X. Feng, X. He, M. Ouyang, L. Lu, P. Wu, C. Kulp, S. Prasser, Thermal runaway propagation model for designing a safer battery pack with 25 Ah $LiNiCoMnO_2$ large format lithium ion battery, Appl. Energy 154 (2015) 74–91.
[62] L. Zhao, I. Watanabe, T. Doi, S. Okada, J. ichi Yamaki, TG-MS analysis of solid electrolyte interphase (SEI) on graphite negative-electrode in lithium-ion batteries, J. Power Sources 161 (2) (2006) 1275–1280.
[63] J.-S. Shin, C.-H. Han, U.-H. Jung, S.-I. Lee, H.-J. Kim, K. Kim, Effect of Li_2CO_3 additive on gas generation in lithium-ion batteries, J. Power Sources 109 (1) (2002) 47–52.